EPTT 2024
Escola de Primavera de Transição e Turbulência

ABCM
Associação Brasileira de Engenharia e Ciências Mecânicas

EPTT-2024-0012
Numerical Investigation of the Backward Facing Step Configuration Using ILES Methodology

Bruno Alvarez Scapin
bruno.scapin@hotmail.com
Guilherme Fuhrmeister Vargas
guilhermef.engenharia@gmail.com
Karina Ruschel
kruschel@gmail.com
Escola Politécnica, PUCRS, Av. Ipiranga 6681, Porto Alegre, 90619-900, RS, Brasil

Edith Beatriz Camano Schettini
beatriz.camano@gmail.com
Instituto de Pesquisas Hidráulicas, UFRGS, Av. Bento Gonçalves 9500, Porto Alegre, 90650-001, RS, Brasil

Abstract. *This study explores the turbulent flow of the Backward Facing Step (BFS) configuration using the Implicit Large Eddy Simulation (ILES) method. We present a comparative analysis of our simulation results against physical outcomes available in the current literature, focusing on the characteristics of recirculation zones and wall shear rates. The ILES formulation showed consistency in replicating flow characteristics for the adopted configuration, and the results exhibited good agreement with published experimental works. Some discrepancies were found for high Reynolds number simulations, which were explained due the definition of the characteristic length of the flow. Coherent structures generated by the turbulent flow, such as Streaks and Hairpin Vortices, were identified. Our study also explored the hydraulic energy of the flux when a well-developed regime is achieved. The calculation of the total head allowed us to compute the friction factor, which showed good agreement with theoretical values. This work contributes to understanding the effects of Reynolds number and geometry on the BFS configuration and can provide a basis for future optimizations in practical applications, such as the design of hydraulic structures and mechanical components.*

Keywords: *Backward Facing Step, Implicit Large Eddy Simulation, Numerical Modelling*

1. INTRODUCTION

The Backward Facing Step (BFS) configuration is a typical experimental setup for flow with separation, used in fluid mechanics to study complex flow patterns and turbulence. It consists of a sudden expansion in a channel that creates recirculation zones downstream from the step. It is often associated with cases such as aerodynamic flows, heat transfer systems, and flows around buildings (Chen *et al.*, 2018). This configuration helps in studying several flow phenomena and their implications in various engineering and environmental contexts.

The study of this configuration contributes to understanding the influence of obstacles on turbulent patterns and the mechanisms governing the formation of vortex and coherent structures, which is a valuable tool for investigating turbulent flow around natural obstacles. It can also provide a basis for studying sediment transport, mixing processes, and optimizing the design of mechanical systems, such as airfoil shapes in aerodynamics and heat exchangers in thermal applications (Lien and Leschziner, 1994; Lu and Zhao, 2018; Zhang *et al.*, 2024). The recirculation zone behind the step mimics the flow patterns around natural obstacles, providing a basis for studying sediment transport, mixing processes, and habitat dynamics in aquatic ecosystems. The occurrence of the recirculation regions of this configuration is induced by the geometric singularity, and can be particularly more significant in channels with small aspect ratios. These zones contribute to the pressure loss of the flow, due to localized energy dissipation, thereby reducing the discharge capacity of the conduit. These localized losses are proportional to the dynamic pressure and the kinetic energy of the fluid.

Despite its simplicity, this geometry leads to a flow characterized by a curved separated shear layer, resulting in a flux with a high level of complexity characterized by the separation and reattachment of the flow at different points. The three-dimensional nature of the backward-facing step configuration is attributed to two distinct qualitative sources, namely the

influence of channel geometry and the dynamics of the flow itself (Tihon *et al.*, 2010). The flux exhibits large vortex structures within the free shear layer, the reverse flow formation, and gradual reattachment of the main flow as it returns to an equilibrium state. On the other hand, the interaction of the shear layer with the wall results in a fluctuation of the characteristic length of the recirculation bubble, which can be displaced downstream or upstream over time.

Considering the flow behavior within the boundary layer, it was assumed that this geometry would similarly exhibit a straightforward flow pattern, featuring a solitary separation region close to the step. (Armaly *et al.*, 1983). Additional recirculation zones can form along the flow, as schematized in Fig. 1 when considering different conditions related to the step height, step slope, and the flow Reynolds number (Re).

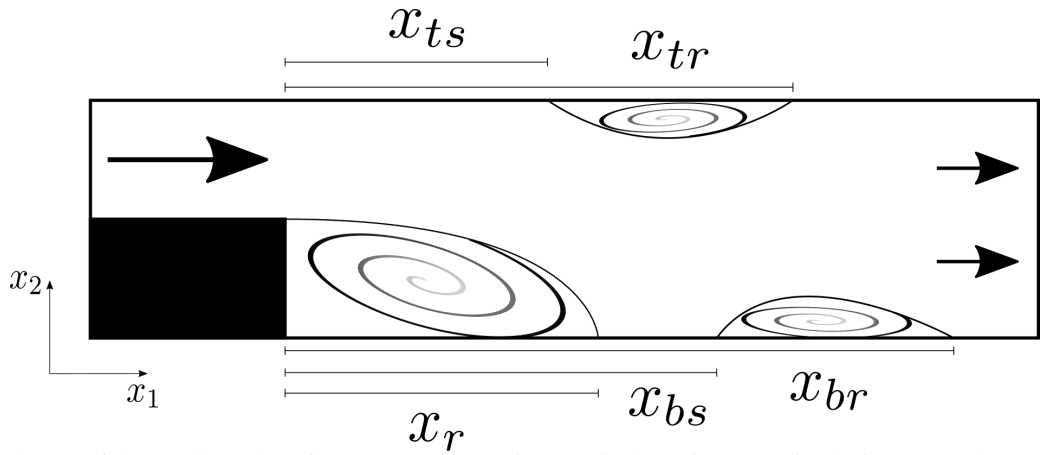

Figure 1: Scheme of the Backward Facing Step configuration. x_r is the primary recirculation reattachment length; x_{bs} and x_{ts} are the position of the flow separation on the bottom and top of the flow, respectively; x_{br} and x_{tr} are the position of the flow reattachment on the bottom and top of the flow, respectively.

The purpose of this work is to show the results of numerical simulations using the Implicit Large Eddy Simulation (ILES) methodology, to investigate the flow response on the BFS configuration. Our results allowed the calculation of the Q-criterion for the fields generated by the ILES simulations, enabling the identification of coherent flow structures. This analysis revealed significant structures, such as Hairpin Vortices and Streaks. We also provide some comparative analysis with experimental data available, focusing on the characteristics of recirculation zones as a function of the Reynolds number. These recirculation zones generated by the step were identified through the flow streamlines, obtained from the velocity fields derived from the simulations. The separation and reattachment were measured with the shear rate results. The results also allowed us to calculate the hydraulic pressure loss of the flow, produced by the wall shear, and subsequently, the friction factor.

2. METHODOLOGY

The simulations were done considering a similar configuration used by Armaly *et al.* (1983) and Tihon *et al.* (2010), for different step Reynolds numbers (Re_h), defined as:

$$Re_h = \frac{\tilde{U}\tilde{h}}{\tilde{\nu}}, \tag{1}$$

where $\tilde{U}$ is the dimensional characteristic velocity, $\tilde{h}$ is the dimensional step height, and $\tilde{\nu}$ is the kinematic viscosity.

To perform the simulations, the Xcompact3D (Bartholomew *et al.*, 2020) solver was used. This open-source tool adopts a high-order scheme, based on the finite difference method.

The solved Navier-Stokes equations for incompressible flow starts as:

$$\frac{\partial \tilde{u}_i}{\partial \tilde{x}_i} = 0, \tag{2}$$

$$\frac{\partial \tilde{u}_i}{\partial \tilde{t}} + \tilde{u}_j \frac{\partial \tilde{u}_i}{\partial \tilde{x}_j} = -\frac{1}{\tilde{\rho}} \frac{\partial \tilde{p}}{\partial \tilde{x}_i} + \tilde{\nu} \frac{\partial^2 \tilde{u}_i}{\partial \tilde{x}_j \partial \tilde{x}_j}, \tag{3}$$

where $\tilde{u}_i$ is the dimensional velocity vector field, $\tilde{p}$ is the dimensional pressure and $\tilde{\rho}$ is the specific mass. Each variable and function is nondimensionalised as following:

$$x_i = \frac{\tilde{x}_i}{\tilde{h}}, \tag{4}$$

$$u_i = \frac{\tilde{u_i}}{\tilde{U}}, \tag{5}$$

$$t = \frac{\tilde{t}\,\tilde{U}}{\tilde{h}}, \tag{6}$$

$$p = \frac{\tilde{p}}{\tilde{\rho}\,\tilde{U}^2}, \tag{7}$$

By substituting Eqs. (4) and (5) in Eq. (2), and Eqs. (1), (4), (5), (6) and (7) in Eq. (3) one can non-dimensionalize the incompressible Navier-Stokes equations. The equations are presented here in their skew-symmetric form, with the diffusive term replaced by the spectral vanishing viscosity (SVV) model (Karamanos and Karniadakis, 2000), in order to introduce the ILES methodology. The resulting non-dimensionalized form is:

$$\frac{\partial u_i}{\partial x_i} = 0, \tag{8}$$

$$\frac{\partial u_i}{\partial t} + \frac{1}{2}\left(u_j\frac{\partial u_i}{\partial x_j} + \frac{\partial u_i u_j}{\partial x_j}\right) = -\frac{\partial p}{\partial x_i} + \frac{1}{Re}\left(\frac{\partial^2 u_i}{\partial x_j \partial x_j} + \frac{\partial}{\partial x_j}\left[Q_c * \frac{\partial u_i}{\partial x_j}\right]\right), \tag{9}$$

where $Re = Re_h$ for our simulations, Q_c is a hyperviscosity kernel, used to construct the model operator through a convolution operation ($*$). Although the hyperviscous kernel is conceptualised in the spectral domain, it can be applied in the physical domain by modifying the numerical scheme.

To approach the aforementioned system of equations, the Xcompact3D solver uses sixth-order centered compact schemes, for spatial discretization (Lele, 1992), and the third-order explicit Adams-Bashforth method, for time advancement (Durran, 1991). The nonlinear term of the momentum equation was computed in skew-symmetric form to reduce aliasing and increase numerical stability (Kravchenko and Moin, 1997). The pressure is computed using the projection method (Chorin, 1968), resulting in a Poisson equation, which is solved in the spectral space using the Fast Fourier Transform (FFT) via the 2DECOMP&FFT package (Li and Laizet, 2010), which contains the FFT algorithm and allows domain decomposition for parallel computation. The Xcompact3D code enables the usage of Implicit Large Eddy Simulation (ILES) and Direct Numerical Simulation (DNS).

The ILES methodology is the approach chosen in our study, based on the extra dissipation included in the numerical approximation of the second derivative. The modification in the numerical scheme mimics the behavior of the spectral vanishing viscosity (SVV) model (Karamanos and Karniadakis, 2000; Lamballais *et al.*, 2011; Dairay *et al.*, 2017; Frantz *et al.*, 2021). The approximation of the derivatives of the diffusion terms of the momentum equation are based on a compact (implicit) finite difference scheme, whose coefficients and stencil size depend on the desired order of accuracy (Lele, 1992). This approximation can be written as follows:

$$\alpha f''_{i+1} + f''_i + \alpha f''_{i-1} \approx a\frac{f_{i+1} - 2f_i + f_{i-1}}{\Delta x^2} + b\frac{f_{i+2} - 2f_i + f_{i-2}}{4\Delta x^2} + c\frac{f_{i+3} - 2f_i + f_{i-3}}{9\Delta x^2} + d\frac{f_{i+4} - 2f_i + f_{i-4}}{16\Delta x^2}, \tag{10}$$

where f_i is the discrete function, f''_i is the second derivative of the discrete function, and Δx is the distance between the evaluated points. The coefficients α, a, b, c, and d are determined accordingly to the accuracy of the second derivative and according to the SVV model constraint equations. To maintain a sixth-order accuracy approximation, the following equations must be satisfied:

$$1 + 2\alpha = a + b + c + d \tag{11}$$

$$\frac{4!}{2!}\alpha = a + 2^2 b + 3^2 c + 4^2 d \tag{12}$$

$$\frac{6!}{4!}\alpha = a + 2^4 b + 3^4 c + 4^4 d \tag{13}$$

forming a system of 3 equations and 5 unknowns. By setting $c = d = 0$, it is mathematically possible to satisfy the aforementioned equations while maintaining sixth-order accuracy using the smallest stencil ($i - 2$ to $i + 2$). In contrast, two additional constraint equations can be proposed to compute the coefficients of the numerical scheme, omitting the previously mentioned trivial solution.

The Fourier analysis of the scheme used produces the modified wave number (κ'') given by:

$$\kappa''(\kappa) = \frac{2a\left[1 - \cos(\kappa\Delta x)\right] + \frac{b}{2}\left[1 - \cos(2\kappa\Delta x)\right] + \frac{2c}{9}\left[1 - \cos(3\kappa\Delta x)\right] + \frac{d}{8}\left[1 - \cos(4\kappa\Delta x)\right]}{\Delta x^2\left[1 + 2\alpha\cos(\kappa\Delta x)\right]}. \tag{14}$$

where κ is the real wave number. A discrete SVV operator is used, allowing extra numerical viscosity to be added at smallest scales (Frantz *et al.*, 2021), which can be expressed as:

$$\nu_{SVV}\left(\kappa,\kappa_c\right)=\begin{cases}0, & \text{if} \quad \kappa<0.3\kappa_c\\ \nu_0\ \exp\left[-\left(\frac{\kappa_c-\kappa}{0.3\ \kappa_c-\kappa}\right)^2\right], & \text{if} \quad 0.3\ \kappa_c\leq\kappa\leq\kappa_c\end{cases} \tag{15}$$

where κ_c is the cut-off wave number. The SVV operator is computed through the product of the Fourier coefficients of the velocity field and the Fourier coefficients of the SVV model kernel given by:

$$\frac{\partial}{\partial x_j}\left[Q_c * \frac{\partial u_i}{\partial x_j}\right]=\sum_{\kappa_0\leq|\kappa|\leq\kappa_c}\kappa^2\hat{Q}_c\hat{u_k}e^{i\kappa x_k}, \tag{16}$$

where k_0 is the threshold wave number at which the SVV model is activated and $\hat{Q}_c$ is given by:

$$\hat{Q}_c(\kappa)=\exp\left[-\left(\frac{\kappa_c-\kappa}{0.3\ \kappa_c-\kappa}\right)^2\right]. \tag{17}$$

To mimic the SVV operator, it is possible to modify the coefficients of the finite difference scheme, maintaining sixth-order numerical accuracy, by adding two more equations as constraints in the coefficient calculation:

$$\kappa_c''=\left(1+\frac{\nu_0}{\nu}\right)\kappa_c^2, \tag{18}$$

$$\kappa_m''=\left(1+0.437\frac{\nu_0}{\nu}\right)\kappa_m^2, \tag{19}$$

where the ratio ν_0/ν expresses the extra numerical viscosity added to the flow.

Adopting Eqs. (11), (12), (13) and by using Eq. (14) with Eqs. (18) and (19), it is possible to explicitly calculate the scheme coefficients, in function of $\nu 0/\nu$, with the following expressions:

$$\alpha=\frac{405\kappa_c''\Delta x^2-1280\kappa_m''\Delta x^2+2736}{810\kappa_c''\Delta x^2-1280\kappa_m''\Delta x^2+288}, \tag{20}$$

$$a=-\frac{4329\kappa_c''\Delta x^2-256\kappa_m''\Delta x^2-1120\kappa_c''\kappa_m''\Delta x^4+2288}{3240\kappa_c''\Delta x^2-5120\kappa_m''\Delta x^2+1152}, \tag{21}$$

$$b=\frac{2115\kappa_c''\Delta x^2-1792\kappa_m''\Delta x^2-280\kappa_c''\kappa_m''\Delta x^4+1328}{405\kappa_c''\Delta x^2-640\kappa_m''\Delta x^2+144}, \tag{22}$$

$$c=-\frac{9}{8}\frac{855\kappa_c''\Delta x^2-256\kappa_m''\Delta x^2-1120\kappa_c''\kappa_m''\Delta x^4+1328}{405\kappa_c''\Delta x^2-640\kappa_m''\Delta x^2+144}, \tag{23}$$

$$d=\frac{198\kappa_c''\Delta x^2+128\kappa_m''\Delta x^2-40\kappa_c''\Delta\kappa_m''\Delta x^4-736}{405\kappa_c''\Delta x^2-640\kappa_m''\Delta x^2+144}. \tag{24}$$

In the code, the intensity of artificial dissipation is regulated by the input parameter ν_0/ν, which should be adjusted according to the grid resolution and the Reynolds number of the simulation. The behavior obtained at small scales for the scheme in question is used here to adjust the level of numerical dissipation near the mesh cutoff, ensuring high precision and virtually no numerical dissipation at large scales without the need of spatial filtering (Lamballais *et al.*, 2011).

2.1 Configuration and Simulation Parameters

In order to replicate similar experimental conditions adopted by Armaly *et al.* (1983) and Tihon *et al.* (2010), a domain with $L_1 = 100$, $L_2 = 2$, and $L_3 = 25$ was adopted, where L_1 is the dimension in the streamwise direction, L_2 is the total height of the domain, and L_3 refers to the spanwise length. The step itself has a streamwise length of $L_{1,s} = 20$ and a height of $L_{2,s} = 1$. The streamwise dimension L_1 was chosen to be sufficiently long both in the step ($x_1 \leq L_{1,s}$) and in the downstream region of the channel ($x_1 > L_{1,s}$), in order to ensure the flow reaches a fully developed regime, which can be indicated by parallel streamlines ($\partial u_i/\partial x_i = 0$). The simulated channel geometry features a spanwise aspect ratio (AR) given by $L_3/L_{2,s} = 25$ for the upstream region, and $L_3/L_2 = 12.5$ for the downstream region. Additionally, the channel exhibits an expansion ratio (ER) of $L_2/L_{2,b} = 2$. Figure 2 presents a schematic of the domain

Table 1: Numerical parameters. The values of n_1, n_2, and n_3 correspond to the number of elements in each Cartesian component.

Simulation	Re_h	Δx_1	Δx_2	Δx_3	n_1	n_2	n_3	Δt	ν_0/ν
ILES0124	124	0.2493	0.1176	0.4902	401	17	51	5×10^{-3}	4.0
ILES0590	590	0.0625	0.0606	0.0623	1601	33	401	1×10^{-3}	4.0
ILES1000	1000	0.0625	0.0606	0.0623	1601	33	401	1×10^{-3}	8.0
ILES1590	1590	0.0625	0.0606	0.0623	1601	33	401	7.5×10^{-4}	16.0

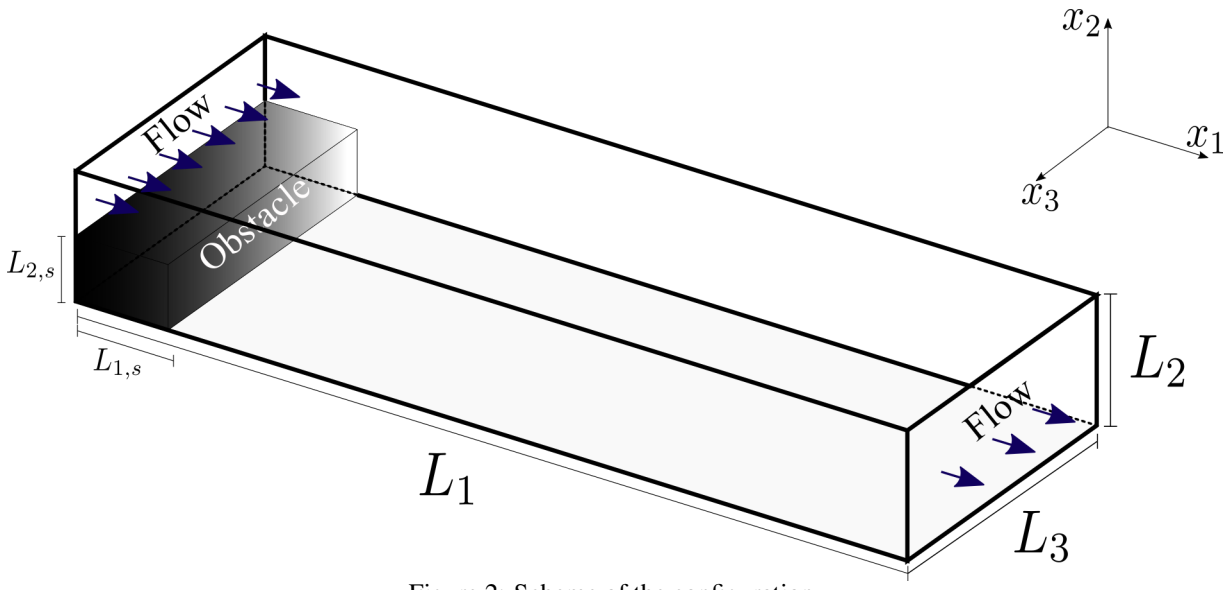

Figure 2: Scheme of the configuration.

used for our simulations. Data related to the hyperviscosity (ν_0/ν) added by the model, as well as the spatial and temporal discretization of the performed simulations, are presented in Tab. 1.

The step was modelled by employing the Immersed Boundary Method (IBM), which allows the representation of complex geometries using a Cartesian grid, without the need to conform the grid to the geometry itself (Schuch, 2020). In order to ensure the no-slip boundary condition at the solid boundary, a one-dimensional expansion using the Lagrange polynomial is used within the solid regions (Gautier *et al.*, 2014). This technique is based on a unidirectional expansion of the solution from the fluid region into the solid, enforcing velocity conditions at the interface, and is compatible with the accuracy of the adopted numerical scheme. It ensures that the flow adheres to the physical constraints imposed by the presence of the step, accurately replicating the interaction between the fluid and the solid surface. This approach simplifies the meshing process and ensures that the boundary conditions are enforced at the interface between the fluid and solid regions.

2.2 Initial and Boundary Conditions

The initial condition for our simulations was:

$$u_i(0, x_1, x_2, x_3) = 0. \tag{25}$$

For $t > 0$, the flow is introduced on the upstream wall ($x_1 = 0$), over the surface above the step, being uniformly distributed on an area of $L_{2,s} \times L_3$. The inlet flow was modelled using the following Dirichlet boundary condition for the velocity field:

$$u_1(t,\ 0,\ x_2,\ x_3) = 1 + I_{noise}\,(2\,X_{rand}(t,\ x_2,\ x_3) - 1)\,, \tag{26}$$

$$u_2(t,\ 0,\ x_2,\ x_3) = I_{noise}\,(2\,X_{rand}(t,\ x_2,\ x_3) - 1)\,, \tag{27}$$

$$u_3(t,\ 0,\ x_2,\ x_3) = I_{noise}\,(2\,X_{rand}(t,\ x_2,\ x_3) - 1)\,, \tag{28}$$

where X_{rand} is an random number that varies between 0 and 1, and I_{noise} is the noise intensity, being for all simulations equal to 0.01. For the downstream wall ($x_1 = L_1$), a convective outlet formulation was used for velocity:

$$\frac{\partial u_i}{\partial t} + U^{b,u}\frac{\partial u_i}{\partial x_j} = 0, \tag{29}$$

where $U^{b,u}$ is the convection velocity, associated with the transport of vortices out of the computational domain. A no slip condition was defined for the spanwise walls, for the top and bottom of the domain, through the following Dirichlet conditions:

$$u_i(t,\ x_1,\ 0,\ x_3) = u_i(t,\ x_1,\ L_2,\ x_3) = u_i(t,\ x_1,\ x_2,\ 0) = u_i(t,\ x_1,\ x_2,\ L_3) = 0. \tag{30}$$

2.3 Post-Processing

In the post-processing section, we divide the analysis into the transient phase, where we study the development and dynamics of the turbulent structures generated by the wall-induced shear and the steady phase, where we analyze the recirculation zones, shear rate, and the resulting head loss of the flow.

2.3.1 Transient phase

For the transient regime analysis, the turbulent structures were identified with the aid of the Q criterion, being a useful quantity to characterize low-pressure structures that are generally associated with coherent vortices (Lesieur *et al.*, 2005). Defining, respectively, the symmetric and antisymmetric parts of the velocity gradient tensor as:

$$S_{ij} = \frac{1}{2}\left(\frac{\partial u_i}{\partial x_j} + \frac{\partial u_j}{\partial x_i}\right), \tag{31}$$

$$\Omega_{ij} = \frac{1}{2}\left(\frac{\partial u_i}{\partial x_j} - \frac{\partial u_j}{\partial x_i}\right), \tag{32}$$

the Q criterion was calculated trough:

$$Q = \frac{1}{2}\left(\Omega_{ij}\Omega_{ij} - S_{ij}S_{ij}\right). \tag{33}$$

2.3.2 Steady phase

Long simulation times were adopted in order to ensure velocity fields in a fully developed regime and steady state, allowing the following temporal averaging:

$$\bar{u}_i = \frac{1}{m}\sum_{n=1}^{m} u_i^n, \tag{34}$$

where m is the number of fields considered for the averaging operation, and n corresponds to the temporal index of the velocity field. The index $n = 1$ is the initial velocity field, where a fully developed regime was identified, and $n = m$ is the index corresponding to the last field obtained from the simulation.

The averaged functions were used to calculate the nondimensionalized wall shear rate at the top and bottom boundaries of the flow. To determine the friction at the bottom and top of the domain, the first numerical derivative of the velocity field at the respective positions was computed during the post-processing stage, using the following equations:

$$\mathcal{S}_b^* = \left.\frac{\partial \bar{u}_1}{\partial x_2}\right|_{x_2=0}, \tag{35}$$

$$\mathcal{S}_t^* = \left.\frac{\partial \bar{u}_1}{\partial x_2}\right|_{x_2=L_2}. \tag{36}$$

For the comparisons, the wall shear rate profiles data presented by Tihon *et al.* (2010) were nondimensionalised considering Eqs. 4 and 5. The wall shear rate was then used to identify the positions of flow separation (x_s) and reattachment (x_r) for the bottom boundary:

$$\mathcal{S}_b^*(x_r) = \mathcal{S}_b^*(x_{bs}) = \mathcal{S}_b^*(x_{br}) = 0, \tag{37}$$

and for the top boundary:

$$\mathcal{S}_t^*(x_{ts}) = \mathcal{S}_t^*(x_{tr}) = 0. \tag{38}$$

The time averaged functions also allowed to calculate the streamline plot of the two-dimensional velocity vector field, given by $\langle u_1\left(x_1,\ x_2,\ x_3 = L_3/2\right),\ u_2\left(x_1,\ x_2,\ x_3 = L_3/2\right)\rangle$, representing curves that are tangent to the velocity vector field at every point, in order to represent the flow. The aforementioned post-processing step allowed the measurement of the end of the primary recirculation zone, also defined as the reattachment length (x_r) and the location of the negative peak

value at the bottom of the flow (x_p) for each case, which were compared to the values presented by Armaly *et al.* (1983), Lee and Matescu (1998), and Tihon *et al.* (2010). Also, a comparative analysis of the locations of the flow separation and the flow reattachment of the secondary recirculation zones at the top (x_{ts} and x_{tr}) and the bottom of the flow (x_{bs} and x_{br}) was done.

The wall exerts resistance against the flow, leading to a frictional pressure drop, which was calculated along with the estimation of the friction factor (f). To determine the linear hydraulic head loss, we calculated the energy at two different points at the step section ($x_1 \leq 20$) and at the downstream region, far from the recirculation zones $x_1 > 50$, in order to avoid the influence on the head loss due the singularity originated by the abrupt change on the geometry.

As dimensional reference values, we use the same values as Tihon *et al.* (2010) being the height of the step $\tilde{h} = 0.01\,m$, the viscosity $\tilde{\nu} = 1{\times}10^{-6}\,m^2 s^{-1}$ and the dimensional velocity given as a function of the simulated step Reynolds number:

$$\tilde{U} = \frac{\tilde{\nu} Re_h}{\tilde{h}}. \tag{39}$$

To establish hydraulic equivalency between circular and rectangular geometries, the hydraulic diameter ($\tilde{D}_h$) is corrected using a geometry function ϕ, as proposed by Jones (1976), which is a function of the channel's aspect ratio and is given by:

$$\phi = \frac{2}{3}\left(1+\frac{s}{w}\right)^2\left(1-\frac{192s}{\pi^5 w}\sum_{n=0}^{\infty}\frac{1}{(2n+1)^5}\tanh\left(\frac{(2n+1)\pi w}{2s}\right)\right). \tag{40}$$

where w is the width of the channel ($w = L_3$), and s is the height of the channel, being $s = L_2/2$ for the step region and $s = L_2$ for the downstream region. For the upstream region, the equivalent hydraulic diameter is calculated by:

$$\tilde{D}_h^* = \phi \tilde{D}_h = \frac{2\phi\,\tilde{L}_2\tilde{L}_3}{\tilde{L}_2 + 2\tilde{L}_3}, \tag{41}$$

while for the downstream region, it is given by:

$$\tilde{D}_h^* = \frac{2\phi\,\tilde{L}_2\tilde{L}_3}{\tilde{L}_2 + \tilde{L}_3}. \tag{42}$$

The mean flow velocity at each point, in function of the streamwise direction, was calculated for the step region ($x_1 \leq 20$) using the following expression:

$$U(x_1) = \frac{2}{L_2\,L_3}\int_0^{L_3}\int_{L_2/2}^{L_2}\bar{u}_1\,dx_2\,dx_3, \tag{43}$$

and the mean pressure was determined by:

$$P(x_1) = \frac{2}{L_2\,L_3}\int_0^{L_3}\int_{L_2/2}^{L_2}\bar{p}\,dx_2\,dx_3. \tag{44}$$

For the downstream region ($x_1 > 20$), as due to the absence of the obstacle, the integration limits are changed, in order to calculate the mean flow velocity and mean pressure:

$$U(x_1) = \frac{1}{L_2\,L_3}\int_0^{L_3}\int_{0}^{L_2}\bar{u}_1\,dx_2\,dx_3, \tag{45}$$

$$P(x_1) = \frac{1}{L_2\,L_3}\int_0^{L_3}\int_{0}^{L_2}\bar{p}\,dx_2\,dx_3. \tag{46}$$

In order to calculate the flow energy at two points, the modified Bernoulli equation was applied (considering the dimensions relevant to the terms of velocity, pressure and height):

$$Y_a\tilde{h} + \frac{(U_a\,\tilde{u})^2}{2\tilde{g}} + \left(P_a\frac{\tilde{u}^2}{\tilde{g}}\right) = Y_b\tilde{h} + \frac{(U_b\,\tilde{u})^2}{2\tilde{g}} + \left(P_b\frac{\tilde{u}^2}{\tilde{g}}\right) + \tilde{H}p_l, \tag{47}$$

where index a and b correspond to two points along the flux (taking into account the fully developed flow), Y is the height of the middle of the flow ($Y = 1.5$ for the upstream region and $Y = 1$ for the downstream region), and $\tilde{H}p_l$ is the dimensional linear head loss due to flow friction with the walls:

$$\tilde{H}p_l = f\frac{\tilde{L}}{\tilde{D}_h^*}\frac{\tilde{U}^2}{2\tilde{g}}, \tag{48}$$

where f is the friction factor, $\tilde{U}$ is the dimensional velocity, $\tilde{L}$ is the distance between the evaluated points. The flow data were correlated as a function of the modified Reynolds number Re^*, which is defined as:

$$Re^* = \frac{\tilde{U}\tilde{D}_h^*}{\tilde{\nu}}. \tag{49}$$

For $Re < 2000$, the friction factor f can be approximated by the following expression:

$$f \approx \frac{64}{Re^*}. \tag{50}$$

2.4 Mesh Convergence Test

Several simulations with different mesh resolution were conducted to analyse the mesh convergence, and justify the choice of the grid discretization presented in Table 1.

For this test, $Re_h = 1590$ was considered, as it requires the finest mesh to accurately capture the flow singularities. This necessity arises because the nonlinearity of the advective term in the equations increases with the Reynolds number.

Given that the numerical scheme used is of third-order accuracy in temporal derivatives and sixth-order in spatial derivatives, the errors associated with temporal approximations are similar to the following order:

$$\varepsilon_t \sim \mathcal{O}(\Delta t^3), \tag{51}$$

while the errors associated with spatial approximations are:

$$\varepsilon_x \sim \mathcal{O}(\Delta x^6). \tag{52}$$

For this test, to ensure that temporal approximation errors do not interfere significantly with the spatial approximation errors in the coarsest components, we use the following criteria:

$$\mathcal{O}(\Delta t^3) \leq \mathcal{O}(\Delta x^6). \tag{53}$$

The discretization parameters for the convergence test are presented in Table 2.

Table 2: Numerical parameters used for the mesh convergence test of $Re_h = 1590$ simulation.

Simulation	Δx_1	Δx_2	Δx_3	n_1	n_2	n_3	Δt	$\mathcal{O}(\Delta x_1^6)$	$\mathcal{O}(\Delta t^3)$
`ILES1590_G0`	0.63	0.20	0.63	161	11	41	5×10^{-2}	$\sim 10^{-2}$	$\sim 10^{-4}$
`ILES1590_G1`	0.35	0.17	0.35	289	13	73	1×10^{-2}	$\sim 10^{-3}$	$\sim 10^{-6}$
`ILES1590_G2`	0.17	0.13	0.17	601	17	151	1×10^{-2}	$\sim 10^{-5}$	$\sim 10^{-6}$
`ILES1590_G3`	0.13	0.13	0.13	801	17	201	1×10^{-2}	$\sim 10^{-6}$	$\sim 10^{-6}$
`ILES1590_G4`	0.08	0.08	0.08	1201	25	301	5×10^{-3}	$\sim 10^{-7}$	$\sim 10^{-7}$
`ILES1590`	0.06	0.06	0.06	1601	33	401	7.5×10^{-4}	$\sim 10^{-8}$	$\sim 10^{-10}$

The location of the peak value of $\mathcal{S}_b^*$, defined as x_p, was calculated for each simulation, and the results are presented in Fig. 3. As we noticed an asymptotic value in function of the grid resolution ($\Delta x_1 < 0.17$), for the highest Re_h simulation, it is assumed that the adopted grid resolution, presented in Table 1, is sufficiently fine in order to represent the flow for the proposed simulations.

3. RESULTS

In this section, the results of the simulations introduced in Tab. 1 are presented and discussed.

3.1 Turbulent Structures

The z-component of the vorticity (ω_z) and the isosurface of the Q criterion ($Q = 5$) were calculated for different time steps of `ILES1590` simulation (Fig. 4), revealing the development of a large transverse vortex in the spanwise direction. This vortex detaches from the step, as seen at $t = 0.25$, and propagates downstream. Initially, the vorticity is concentrated near the step, marking the early stages of structure formation. As the simulation progresses, the detached vortex continues its downstream propagation. The breakdown of the large elongated vortex leads to the formation of an additional transverse structure ($t = 8.25$), which exhibits more complex structures and finer details. Both vortices are counter-rotating, as indicated by the ω_z values. The influence of the spanwise walls ($x_3 = 0$ and $x_3 = L_3$) becomes apparent as they decelerate the coherent structures. As the transverse structures propagate, they thin out and eventually break down into numerous smaller, longitudinal structures. By time $t = 12$, these have traveled further downstream, and

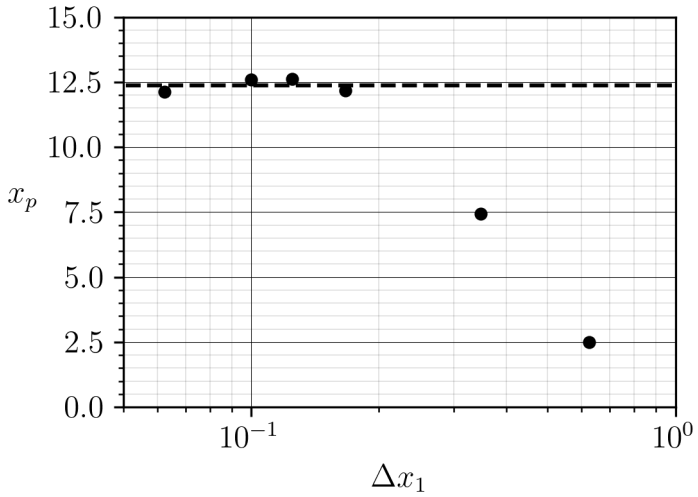

Figure 3: Mesh convergence test for $Re_h = 1590$.

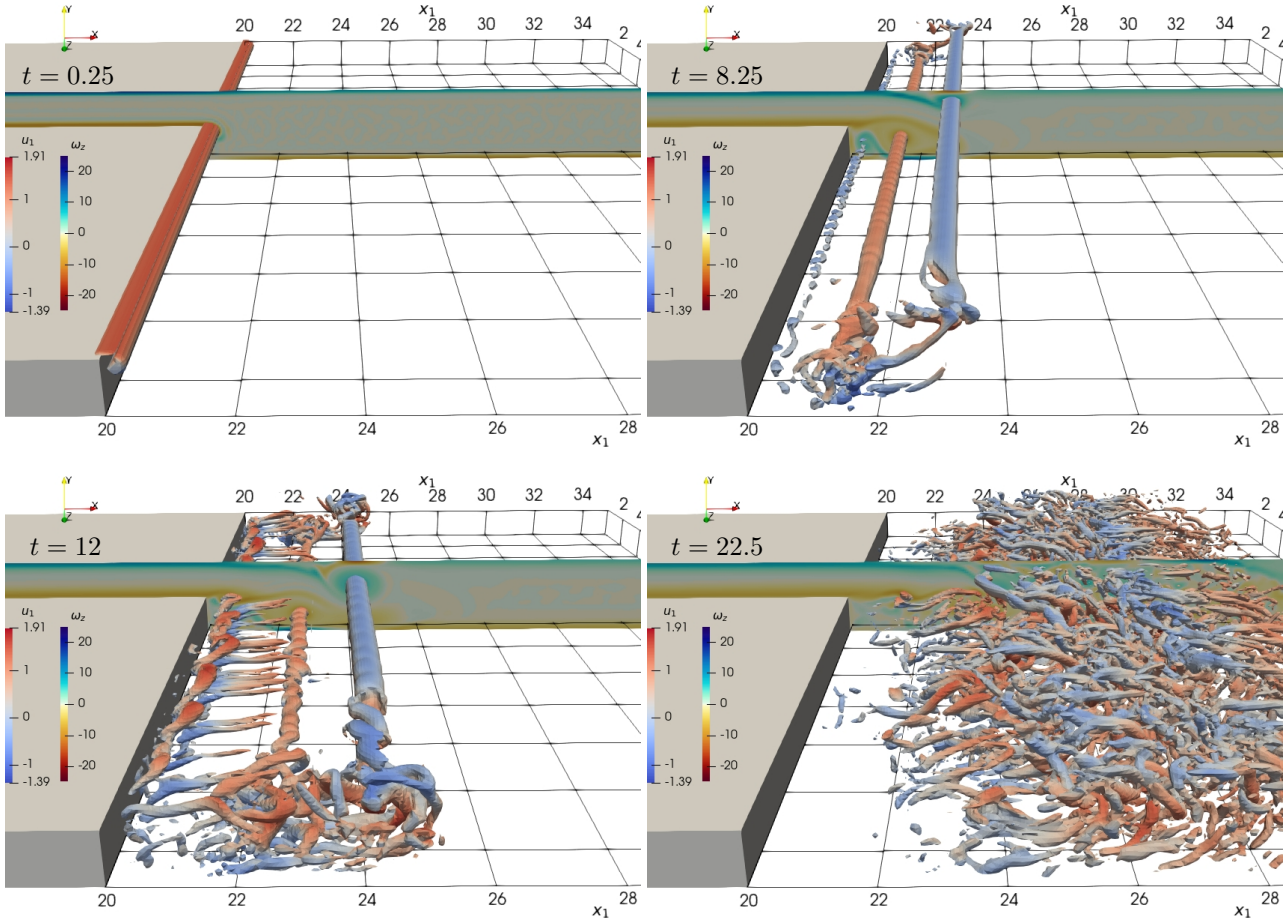

Figure 4: Isocontours of Q criterion ($Q = 5$) and the z component of the vorticity field (ω_z) obtained from `ILES1590` simulation.

their interactions have grown increasingly complex. The no-slip condition at the bottom of the flow generates numerous elongated structures behind the step, that propagate downstream, likely contributing to the formation of hairpin vortex-like structures. A noticeable rise in the number of structures is observed in $t = 22.5$, which appear more intertwined and elongated, signifying the development of more complex flow dynamics. At this time step, the flow has transitioned into a highly turbulent state. The spanwise no-slip condition further contributes to the breakdown of these structures, leading to the generation of numerous smaller structures. The vortical structures have further fragmented, resulting in a chaotic mix of smaller-scale vortices. This stage likely represents the fully turbulent regime, characterized by intense mixing and

complex interactions among the vortices.

Figure 5 present the isosurface of the Q criterion ($Q = 1$), highlighting the turbulent structures modelled in the `ILES0590` simulation. At $t = 15$, numerous transverse vortices have formed and are moving downstream at varying

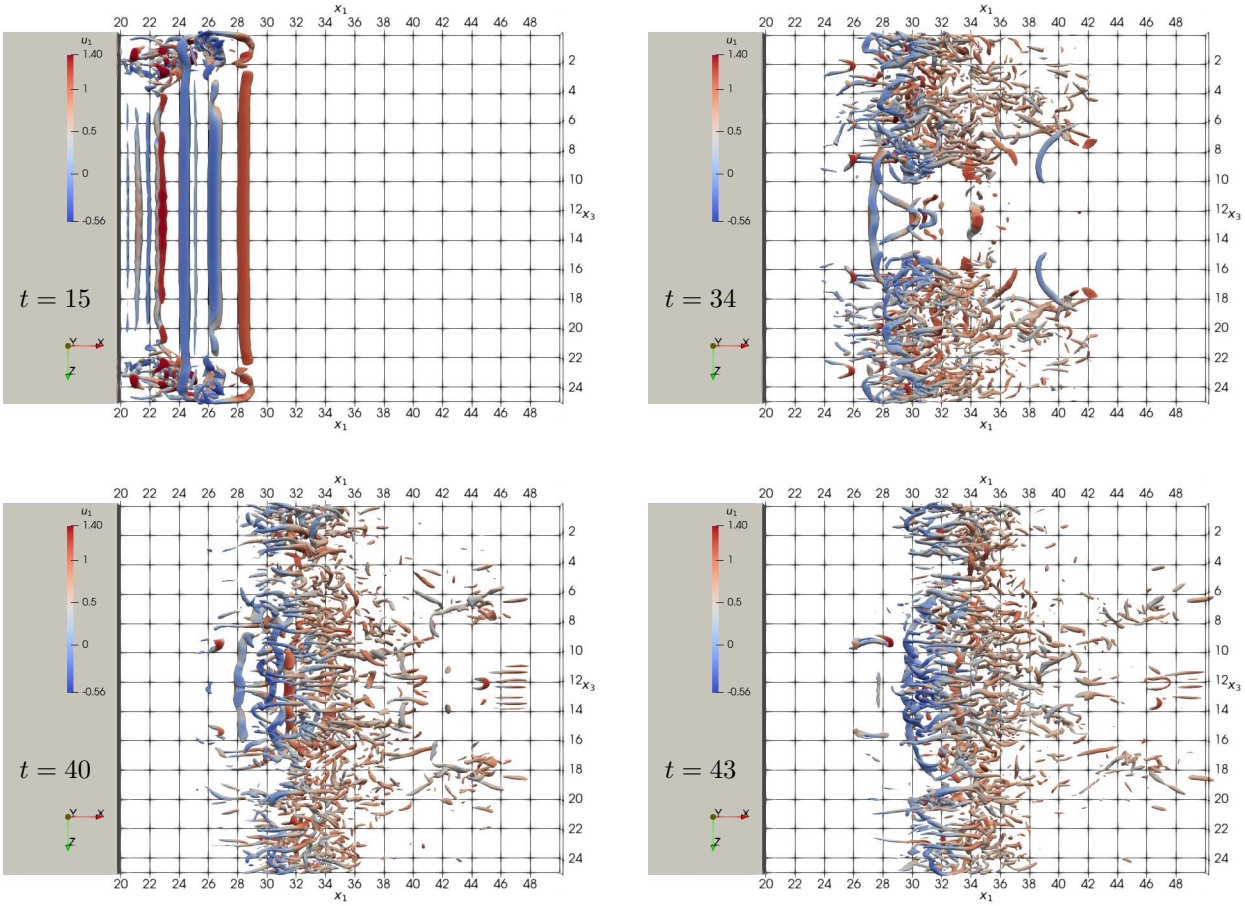

Figure 5: Isocontours of Q criterion ($Q = 1$) and the z component of the vorticity field obtained from `ILES590` simulation.

velocities. The structures progressively thin as they approach the step. As the simulation advances to $t = 34$, these coherent structures begin to interact, becoming more complex, with the flow showing clear signs of transitioning towards turbulence. It can be observed well-defined Hairpin vortices behind numerous elongated structures forming along the streamwise direction (Fig. 6). In Fig. 7, the results from the `ILES0590` case clearly highlight the formation of elongated curved tube-like structures in the streamwise direction, known as Streaks. These are counter-rotating longitudinal structures that form near the bottom, as described by Hussain (1983). Near these structures, the formation of hairpin vortices, can be observed, which move downstream while being stretched until they dissipate. The well-defined streaks observed at earlier times have evolved into more complex structures, with a noticeable increase in the density of vortical formations. By $t = 40$ and $t = 43$, the flow has entered a fully turbulent state, characterized by a dense and chaotic mix of small-scale vortical structures. The coherent structures from earlier time steps have largely broken down into smaller vortices, indicating widespread turbulence throughout the flow field. As expected, a higher number of coherent structures can be observed for the higher Reynolds number case, which are more complex and exhibit a stronger 3D character compared to those formed at the lower Re_h.

3.2 Shear Stress

The simulations results enabled the calculation of the shear stresses at the top ($\mathcal{S}_t^*$) and bottom walls ($\mathcal{S}_b^*$), and subsequently the exact measurement of the primary reattachment length (x_r), the position of the flow separation on the bottom and top of the flow (x_{bs} and x_{ts}), the position of the flow reattachment on the bottom and top of the flow (x_{br} and x_{tr}), and the position of the negative peak in wall shear stress at the bottom of the flow (x_p).

The comparisons of both bottom and top wall shear rates, for the $Re_h = 124$ case, are presented in Fig. 8 and Fig. 9. The shear stress values at both positions showed good agreement with the experimental results of the reference author, with a local minimum observed at $x_1 \approx 3.5$ for the bottom wall and $x_1 \approx 6$ for the top wall. Additionally, a small

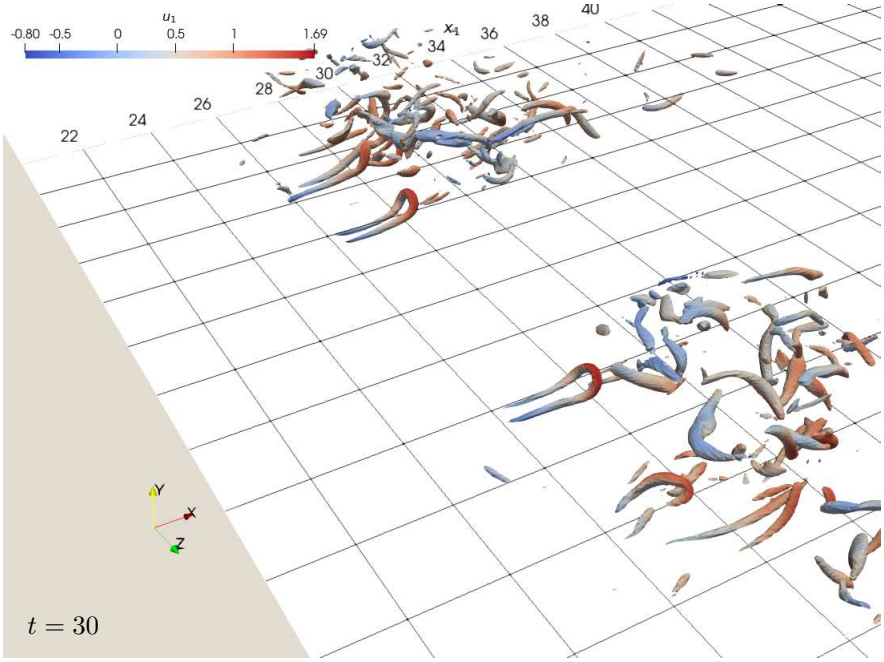

Figure 6: Hairpin vortices structures, generated in `ILES0590` for $t = 30$.

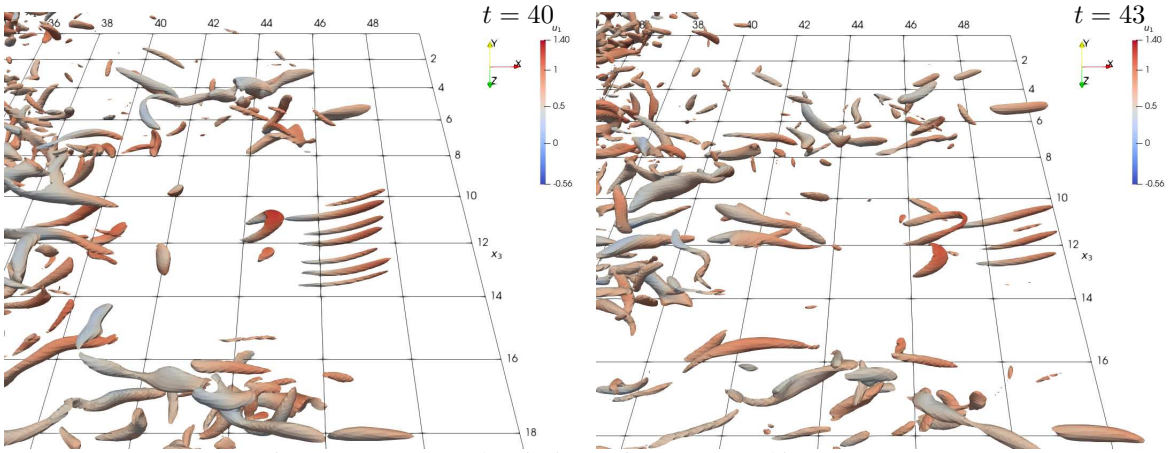

Figure 7: Streaks and Hairpin vortices generated in `ILES0590`.

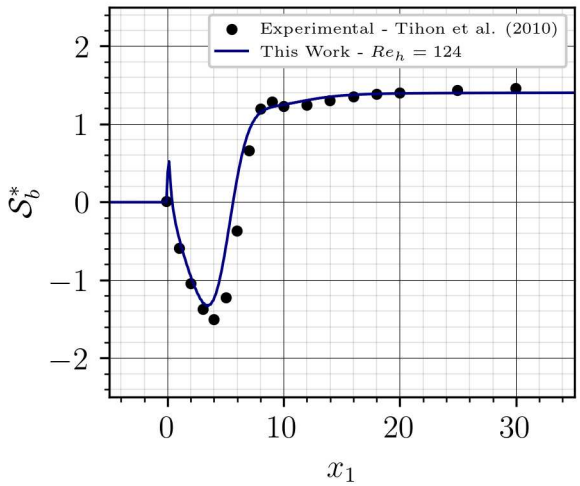

Figure 8: Bottom wall shear stress from the `ILES0124` simulation.

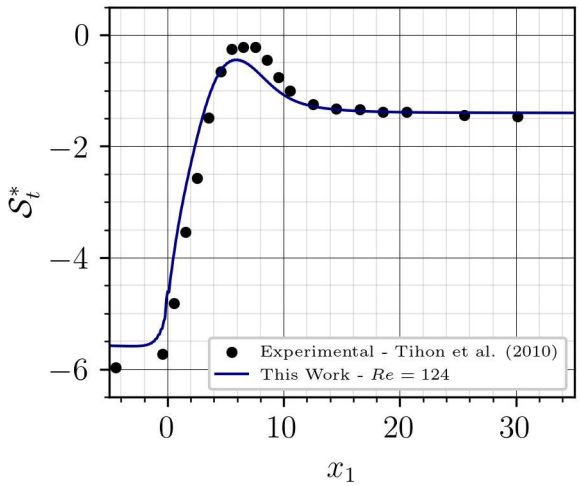

Figure 9: Top wall shear stress from the `ILES0124` simulation.

secondary recirculation region was identified on the bottom wall, extending from $x_1 = 0$ to $x_1 \approx 0.3$. As the flow stabilizes and becomes fully developed, the shear stress values for both the top and bottom walls tend to stabilize at a constant value as a function of x_1, which can be observed for $x_1 > 25$.

Figures 10 and 11 present the bottom and top shear stress profiles obtained for the $Re_h = 590$ case. The results

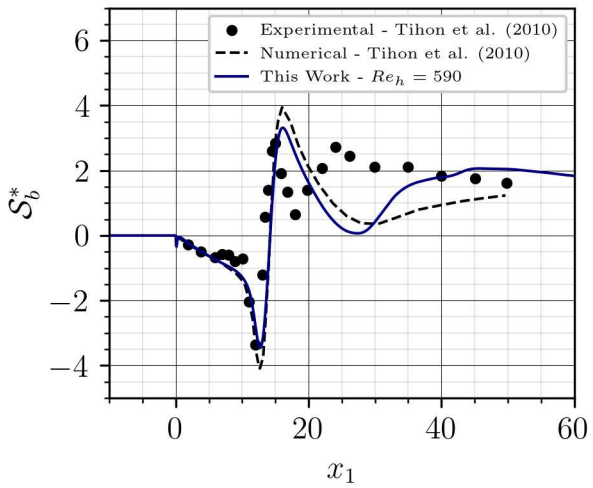

Figure 10: Bottom wall shear stress from the `ILES0590` simulation.

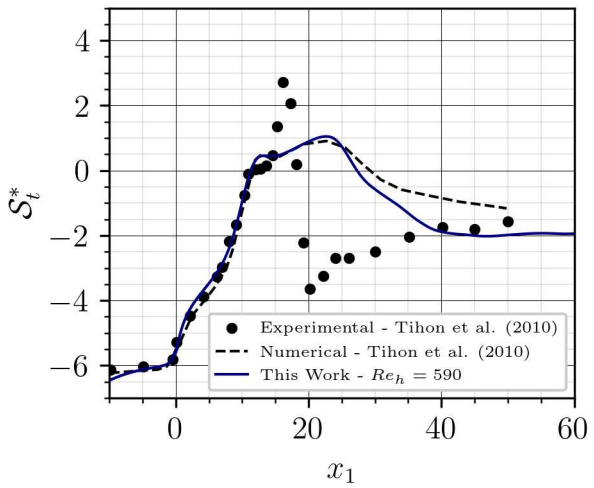

Figure 11: Top wall shear stress from the `ILES0590` simulation.

showed good agreement with the numerical results reported by Tihon *et al.* (2010). The positions of the global maximum and minimum of the bottom shear stress closely matched with the numerical simulations of Tihon *et al.* (2010) and they reasonably corresponded with the experimental observations. The local minimum was found at approximately at $x_1 \approx 13$. At $x_1 \approx 27$, the near formation of a secondary recirculation zone at the bottom of the flow was observed. The top shear stress results for `ILES0590` were close to those of the reference author in the region between $-10 < x_1 < 15$. Beyond this range, our results reasonably matched the reference authors numerical simulation.

The bottom and top shear stress results for the $Re_h = 1000$ case are presented in Figures 12 and 13. In the bottom

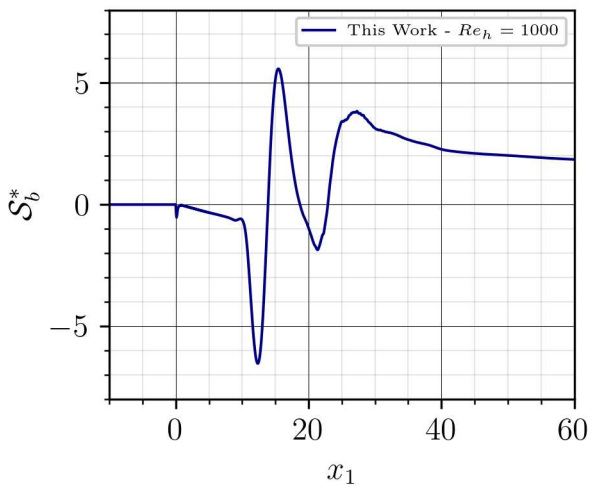

Figure 12: Bottom wall shear stress from the `ILES1000` simulation.

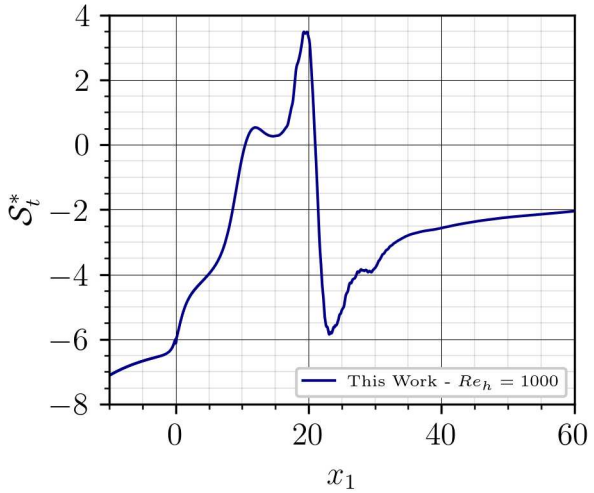

Figure 13: Top wall shear stress from the `ILES1000` simulation.

of the channel, the primary recirculation zone can be identified between $x_1 = 0$ and $x_1 \approx 12$, with the emergence of a secondary recirculation zone extending from $x_1 \approx 19$ to $x_1 \approx 23$. At the top of the domain, the secondary recirculation zone spans from $x_1 \approx 10$ to $x_1 \approx 20$.

The shear stress profiles for the `ILES1000` simulation (Fig. 12 and Fig. 13) exhibit a similar shape to those obtained for the reference authors $Re_h = 590$ experiment (Fig. 10 and Fig. 11), both at the top and bottom boundaries. For the bottom shear rate, there is the presence of an abrupt global maximum and minimum in $x_1 \approx 12$, $x_1 \approx 16$, respectively, aligning with $Re_h = 590$ experimental outcomes. Subsequently, a local minimum and maximum occur before the onset

of a fully developed flow. The top shear stress profile also reflects this behavior as a function of x_1, emphasising the consistency between the two cases. This similarity suggests that there might be a variation in the methodology used to determine appropriate the flow Reynolds number. In our simulations, Re_h was adopted based on the step height, following the definition used by Tihon *et al.* (2010). However, significant variations in the Reynolds number due to the appropriate characteristic length and geometric shape should be considered. This indicates that the shear stress profile is highly sensitive to how the flow Reynolds number is defined.

The results for $Re_h = 1590$ are illustrated in Figures 14 and 15. The shape of the wall shear stress function at the

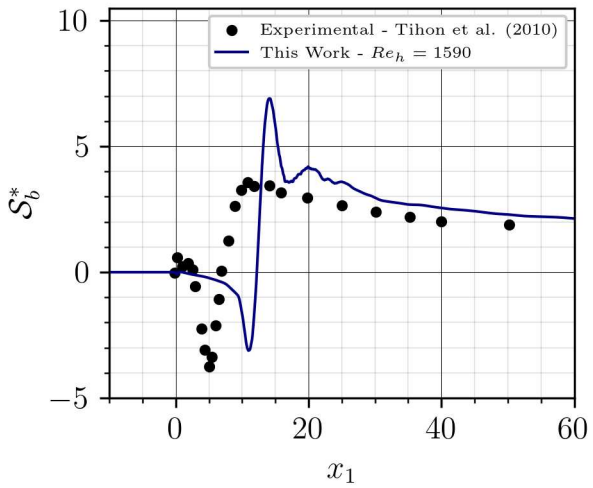

Figure 14: Bottom wall shear stress from the `ILES1590` simulation.

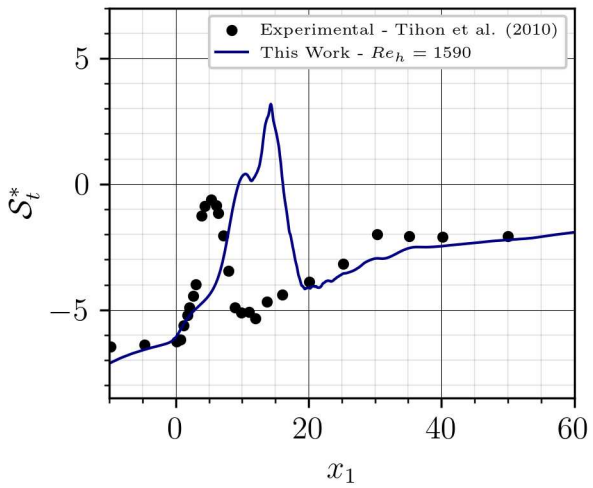

Figure 15: Top wall shear stress from the `ILES1590` simulation.

bottom of the channel changed significantly compared to the `Re1000` simulation, as the local maxima and minima were smoothed out before the onset of a fully developed flow regime. A global minimum and maximum were identified at $x_1 \approx 11$ and $x_1 \approx 14$, respectively. The obtained results deviated from those of the reference author, as it is evident that the positions of the separation and reattachment zones in both cases were offset compared to the reference results.

3.3 Characteristics of Recirculation Zones

Using a central plane at $x_3 = L_3/2$, streamlines were obtained through the mean velocity fields $\bar{u}_1$ and $\bar{u}_2$. These results allow the identification of the recirculation zones generated by the flow.

For simulation `ILES0124` (Fig. 16), a zone of flow separation is nearly observable at the top of the domain, around $x_1 \approx 7$. The flow appears to be well-developed throughout most of the domain, and it can be reasonably assumed that the flow is fully developed for $x_1 > 20$, where the streamlines become parallel.

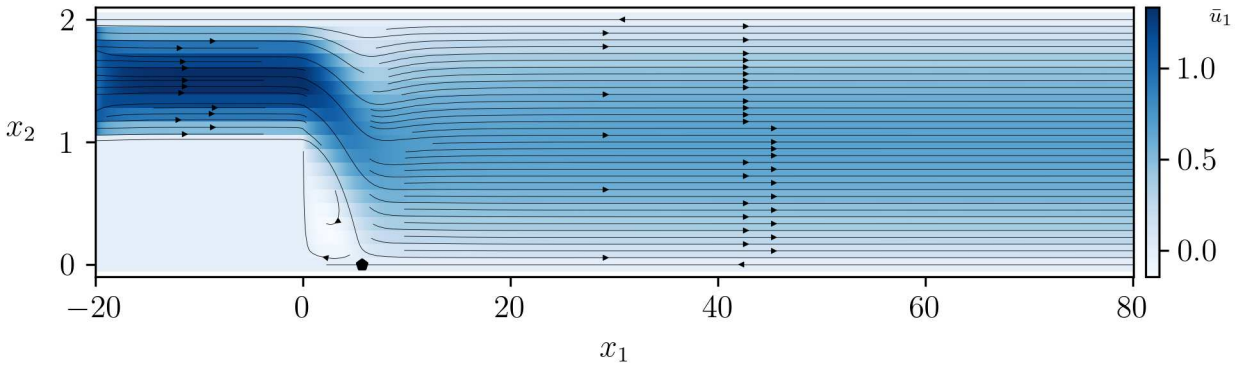

Figure 16: Results of Flow lines from `ILES0124` simulation.

The results for the `ILES0590` case highlight the formation of the recirculation zone at the top of the domain, beginning at $x_{ts} \approx 11$ and ending at $x_{tr} \approx 27$, while the primary recirculation reattaches at $x_r \approx 14$, as shown in (Fig. 17). The increase in Re_h led to a longer flow development length downstream of the step. The region where the flow remains undeveloped and is influenced by the recirculation zone attached to the step is broader compared to the `ILES0124` simulation, extending across the interval $0 < x_1 < 50$.

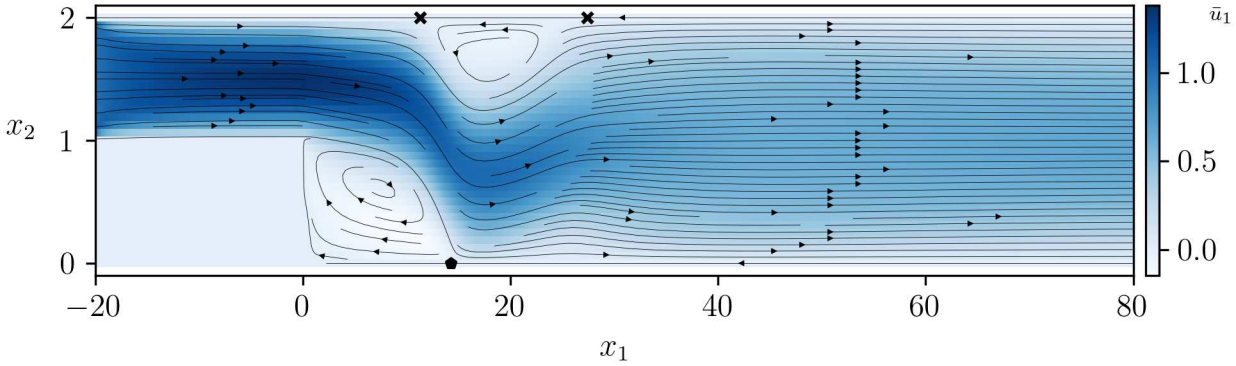

Figure 17: Results of Flow lines from `ILES0590` simulation.

In the `ILES1000` simulation (Fig. 18), further downstream from the primary recirculation zone, the onset of a small secondary recirculation zone is observed in the bottom of the channel, marked by the separation of streamlines from the bottom of the channel. The low magnitude of the peak in $\mathcal{S}_b^*$ (Fig. 12) justify the small size of this recirculation bubble.

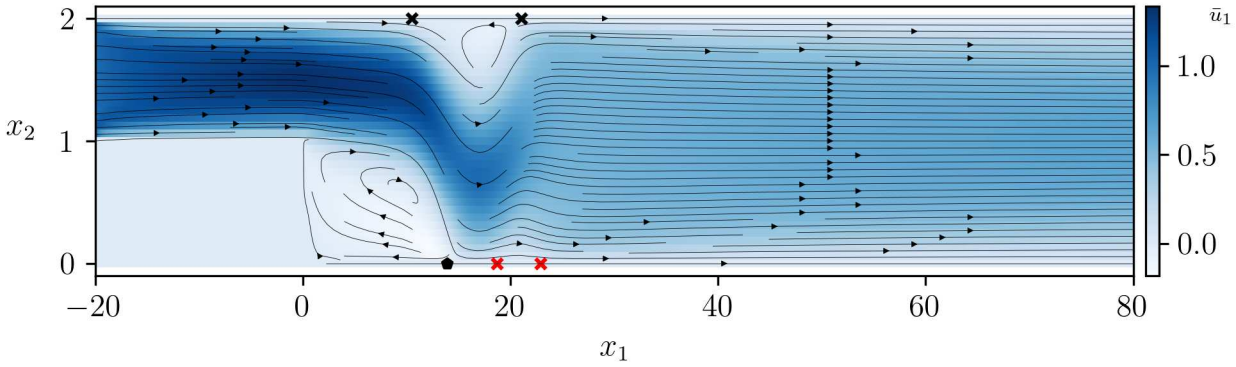

Figure 18: Results of Flow lines from `ILES1000` simulation.

In the `ILES1590` simulation results, the secondary bottom recirculation zone is no longer noticeable, similar to what was documentated by Armaly *et al.* (1983). The primary recirculation zone shrinks, with $x_r \approx 12$ and it is almost noticeable a secondary recirulation zone next to the step ($x_1 \approx 0$). A similar shrinking effect is noticeable in the top recirculation zone ($x_{ts} \approx 10$ and $x_{tr} =\approx 16$). The flow also stabilizes at a more upstream position compared to the

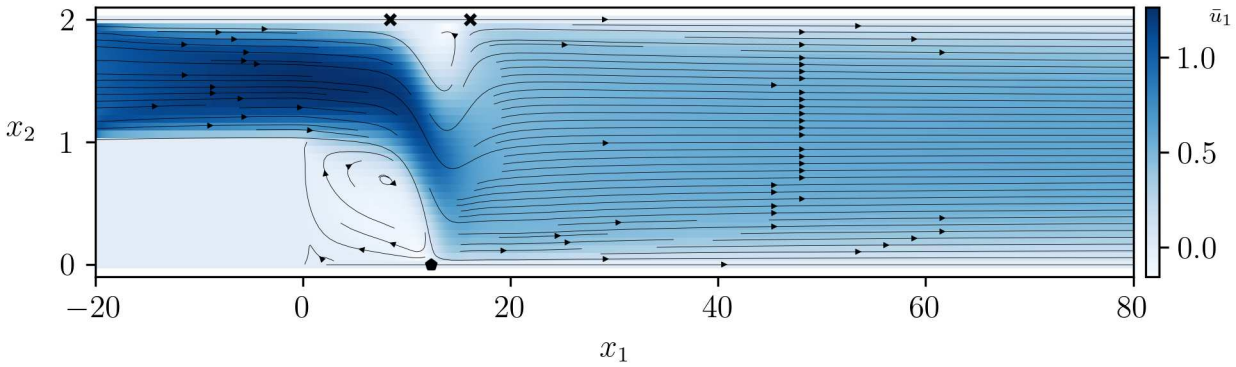

Figure 19: Results of Flow lines from `ILES1590` simulation.

`ILES1000` simulation, due to the absence of the secondary recirculation zone at the bottom.

The results related to the position of separation and reattachment points were then compared with the experimentally observed values reported by Armaly *et al.* (1983), Lee and Matescu (1998), and Tihon *et al.* (2010), as presented in Fig. 20. The obtained ratio between the primary reattachment length and the position of the negative peak value of wall shear stress (x_r/x_p) approached those presented by Tihon *et al.* (2010) for simulations `ILES0124`, `ILES0590` and `ILES1000`, however our observed outcome of simulation `ILES1590` deviated from that obtained by the reference author. For Re_h values ranging from 0 to 590, the primary reattachment length (x_r) shows satisfactory convergence with all

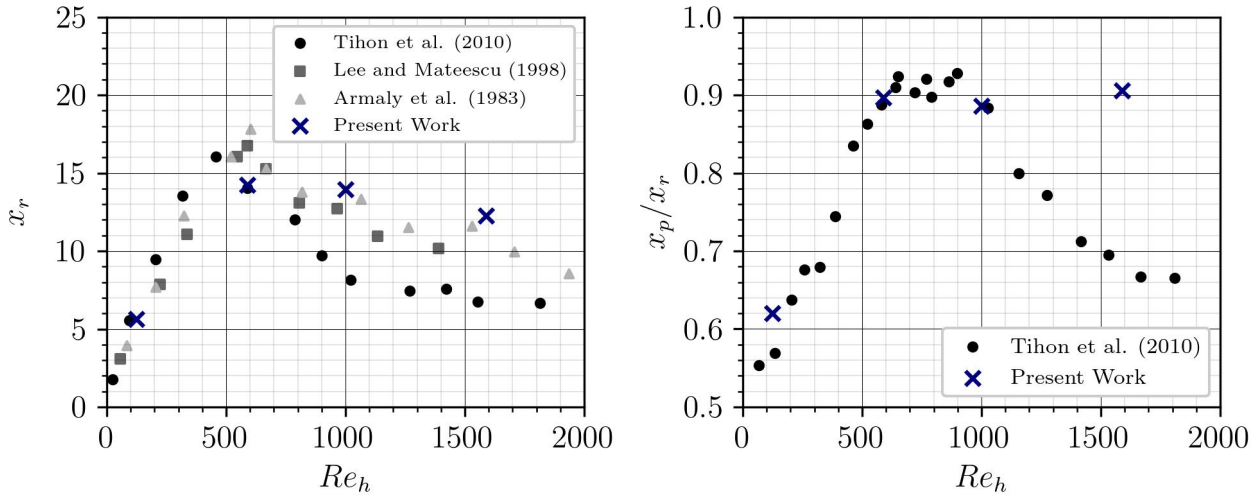

Figure 20: Influence of the step Reynolds number over the reattachment length and bottom shear stress. Left: Variation of the primary reattachment length (x_r) with the step Reynolds number (Re_h). Right: Variation of the ratio between the position of the negative peak value of wall shear stress and the primary reattachment length (x_p/x_r) with the step Reynolds number (Re_h).

the reference studies. In contrast, for $Re_h = 1000$ and $Re_h = 1590$, although there was a notable divergence from the findings of Tihon *et al.* (2010), the trend of the results approximated those reported by Armaly *et al.* (1983) and Lee and Matescu (1998). According to the Tihon *et al.* (2010), in the laminar flow interval ($Re_h < 500$) the obtained data agreement is very good, although for higher Re_h the measured $\tilde{x}_r/\tilde{h}$ values exhibit sensitivity to the specific channel geometries which were slightly divergent comparing with the other authors.

A comparative analysis of the locations of the beginning and end of the secondary recirculation zones at the top (x_{ts} and x_{tr}) and the bottom of the flow (x_{bs} and x_{br}) is presented in Fig. 21. The results for the simulation $Re_h = 124$

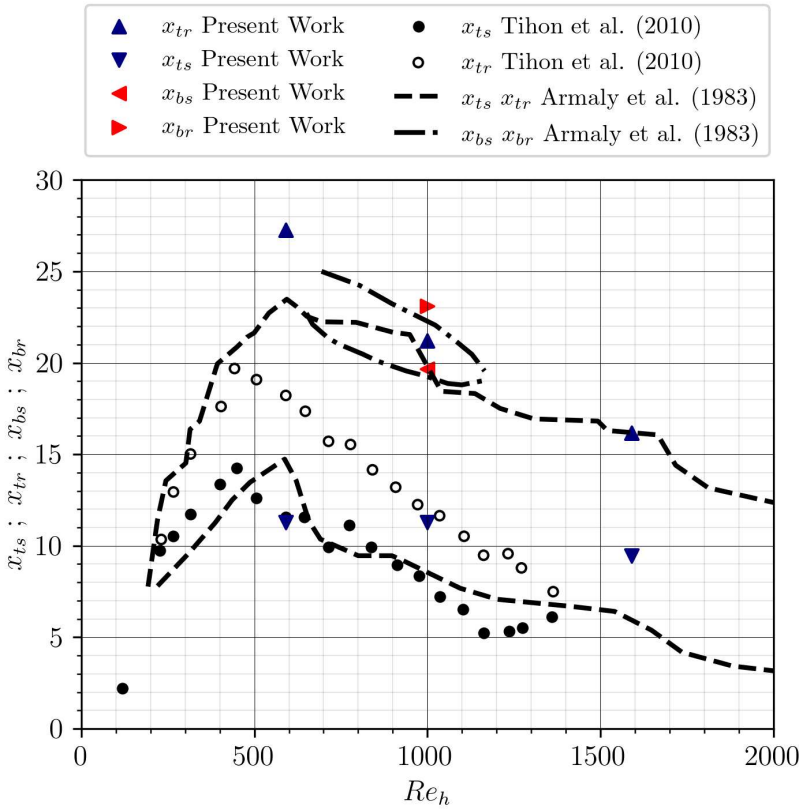

Figure 21: Results of the location of the reattachment and separation of the bottom and top recirculation zones (x_{ts}, x_{tr}, x_{bs}, and x_{br}) in function of Re_h.

significantly diverged from those reported by Tihon *et al.* (2010), where we observe a secondary top recirculation zone formed further the step. In the case of $Re_h = 590$, the results for x_{ts} were close to both reference studies.

Additional regions of flow separation downstream was identified in the top wall for $Re_h = 1000$, aligning with the findings of Armaly *et al.* (1983). As Re_h increases, our results tend to reproduce the trend obtained by Armaly *et al.* (1983) and diverge from those obtained by Tihon *et al.* (2010). This behaviour can be explained due to the definition of the flow Reynolds number, as it was aforementioned.

3.4 Friction Factor

The calculated total hydraulic head ($\tilde{H}$) from the `ILES1590` simulation is presented in Fig. 22. The results show

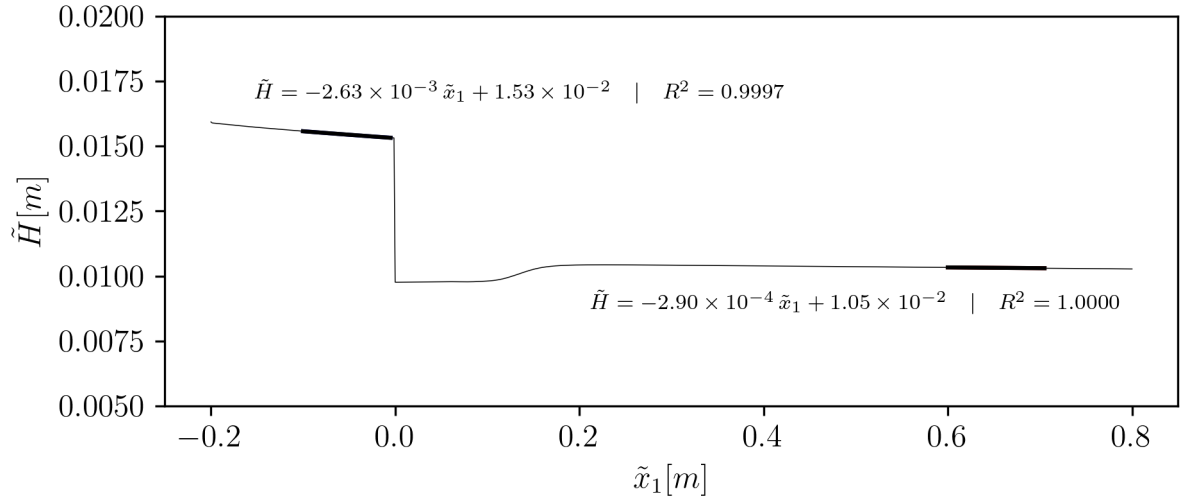

Figure 22: Total hydraulic head results from `ILES1590` simulation.

a decrease in hydraulic head along the channel as a function of the streamwise position ($\tilde{x}_1$), with two linear trending regions, highlighting the energy loss caused due to wall friction. The two distinct linear regions with different slopes are evident: one upstream and the other downstream of the step. Within these regions, the total hydraulic head results were fitted by linear functions, which showed excellent agreement with the simulated data ($R^2 = 0.9997$ and $R^2 = 1.0000$ for the upstream and downstream regions, respectively). The nearly perfectly linear behaviour of the hydraulic head for both sections, in function of $\tilde{x_1}$, highlights the evolution of a well-developed flow where the head loss is fully caused by the wall-induced shear. Between $\tilde{x}_1 = 0$ and $\tilde{x}_1 \approx 0.2$ it is possible to notice an abrupt hydraulic energy loss, caused due to the formation of the recirculation zones generated by the geometric singularity.

Figure 23 illustrates the variation of the friction factor (f) in function of the geometry-corrected Reynolds number (Re^*) for both upstream and downstream regions of the flow. Our results were compared with the theoretical geometry-corrected friction factor, $f = 64/Re^*$, used for laminar flow. The friction factor decreases with increasing Reynolds number, consistent with the expected behavior for laminar and transitional flows. The close alignment of the data points for both upstream and downstream regions with the theoretical curve indicates that the methodology accurately captures the effects of friction in the BFS configuration, despite the complexity introduced by the step.

4. CONCLUSION

The present study employed the Implicit Large Eddy Simulation (ILES) methodology to model the Backward Facing Step (BFS) configuration, demonstrating consistency with established experimental and numerical results. The investigation of recirculation zones and turbulent structures provided valuable insights into the complex fluid dynamics associated with varying Reynolds numbers. The ILES methodology satisfactorily modeled the BFS configuration, and the results enabled the analysis of quantities related to the shear stress generated by the channel walls, recirculation zones, separation and reattachment points, coherent structures and friction factor.

Our simulations captured coherent structures of turbulent flow, such as Hairpin Vortices and Streaks, observed moving downstream, interacting and generating chaotic patterns. The three-dimesionality of the simulations was highlighted by the influence on the generation and motion of the coherent structures, which become more numerous as the Reynolds number increases. The study of the spanned recirculation zones showed that, contrary to what might be intuitively expected, increasing the Reynolds number does not always lead to more recirculation zones. For instance, while a secondary recirculation zone was observed for $Re_h = 1000$ at the bottom of the channel, this zone did not appear for $Re_h = 1590$, consistent with the findings of Armaly *et al.* (1983). The results also enabled the calculation of the total hydraulic energy,

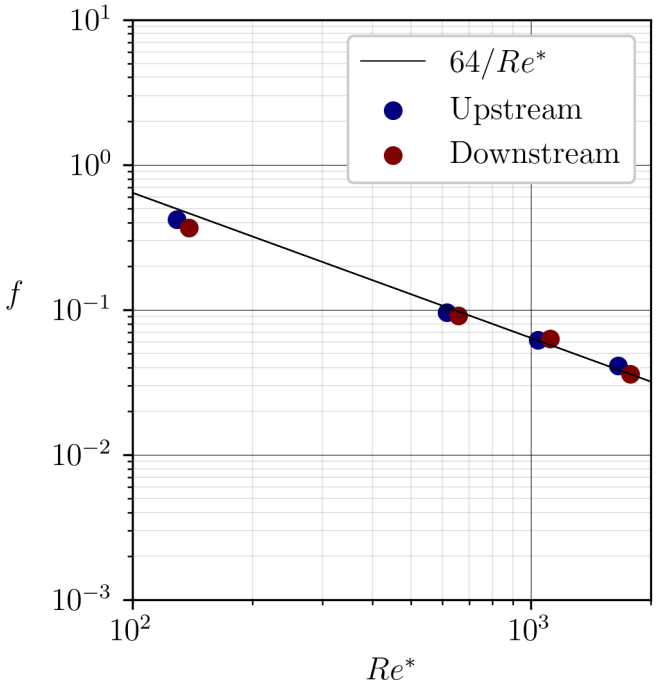

Figure 23: Calculated friction factor for `ILES0124`, `ILES0590`, `ILES1000` and `ILES1590` simulations.

and subsequently of the friction factor by applying a geometric correction factor to reconcile the principles of circular pipe hydraulics with those of rectangular conduits. Our results exhibited good agreement with theoretical predictions related to the friction factor.

The analysis revealed that, while the ILES method accurately captured the primary flow features, there were some deviations at higher Reynolds numbers, which highlighted the sensitivity of flow behavior to geometric variations. For lower Reynolds numbers, the results indicated strong agreement with the literature, while for higher Reynolds numbers, there were significant deviations from experimental data, particularly in the positions of maximum and minimum shear stress. Although the results of our `ILES0590` simulation did not closely match the experimental outcomes of Tihon *et al.* (2010) for $Re_h = 590$, the `ILES1000` results exhibited notable similarities in shear rates to those at $Re_h = 590$, indicating a consistent pattern of the flow behaviour in function of the flow Reynolds number. These deviations can be explained by the strong influence of channel geometry on the flow, which affects the definition of the Reynolds number, as the hydrodynamics are highly sensitive to this parameter. By adopting the hydraulic diameter and introducing the geometric correction factor, as used to calculate the friction factor, could be a valuable approach to reconcile the discrepancies between the experimental results and our numerical simulations, aligning them more closely by accounting for variations in the characteristic length scale.

Future work should focus on a more detailed analysis of pressure loss associated with the geometric singularity of the step, investigating the contribution of the abrupt change in geometry to the energy dissipation. Additionally, extending the study to different step heights and shapes could help in optimizing designs in engineering applications where such geometries are used, including the design of hydraulic drainage structures, such as spillways and culverts, where efficient flow management is critical to prevent erosion and structural damage. Moreover, insights gained from this study could be applied to the design of mechanical components in heat exchangers, where managing turbulent flow and minimizing pressure drop are essential for enhancing thermal performance and energy efficiency.

5. ACKNOWLEDGEMENTS

This work was conducted at the Laboratório de Simulação de Escoamentos Turbulentos (LaSET/PUCRS) as part of the MECT research project, with financial support from Petrobras and CAPES. The simulations were performed using the computational resources of the Laboratório de Alto Desempenho (LAD/PUCRS) and the Santos Dumont supercomputers. The authors also acknowledge the Laboratório Nacional de Computação Científica (LNCC/MCTI, Brazil) for providing access to the SDumont supercomputer, which contributed in achieving the research results.

6. REFERENCES

Armaly, B.F., Durst, F., Pereira, J.C.F. and Schönung, B., 1983. "Experimental and theoretical investigation of backward-facing step flow". *Journal of Fluid Mechanics*, Vol. 127, No. 1, p. 473. ISSN 1469-7645. doi: 10.1017/s0022112083002839.

Bartholomew, P., Deskos, G., Frantz, R.A., Schuch, F.N., Lamballais, E. and Laizet, S., 2020. "Xcompact3d: An open-source framework for solving turbulence problems on a cartesian mesh". *SoftwareX*, Vol. 12, p. 100550.

Chen, L., Asai, K., Nonomura, T., Xi, G. and Liu, T., 2018. "A review of backward-facing step (bfs) flow mechanisms, heat transfer and control". *Thermal Science and Engineering Progress*, Vol. 6, pp. 194–216. ISSN 2451-9049. doi: https://doi.org/10.1016/j.tsep.2018.04.004.

Chorin, A.J., 1968. "Numerical solution of the navier-stokes equations". *Mathematics of Computation*, Vol. 22, No. 104, p. 745762. ISSN 1088-6842. doi:10.1090/s0025-5718-1968-0242392-2.

Dairay, T., Lamballais, E., Laizet, S. and Vassilicos, J.C., 2017. "Numerical dissipation vs. subgrid-scale modelling for large eddy simulation". *Journal of Computational Physics*, Vol. 337, pp. 252–274.

Durran, D.R., 1991. "The third-order adams-bashforth method: An attractive alternative to leapfrog time differencing". *Monthly Weather Review*, Vol. 119, No. 3, p. 702720. ISSN 1520-0493. doi:10.1175/1520-0493(1991)119<0702:ttoabm>2.0.co;2.

Frantz, R.A.S., Deskos, G., Laizet, S. and Silvestrini, J.H., 2021. "High-fidelity simulations of gravity currents using a high-order finite-difference spectral vanishing viscosity approach". *Computers & Fluids*, Vol. 221, p. 104902. ISSN 0045-7930. doi:https://doi.org/10.1016/j.compfluid.2021.104902.

Gautier, R., Laizet, S. and Lamballais, E., 2014. "A dns study of jet control with microjets using an immersed boundary method". *International Journal of Computational Fluid Dynamics*, Vol. 28, No. 610, p. 393410. ISSN 1029-0257. doi:10.1080/10618562.2014.950046. URL `http://dx.doi.org/10.1080/10618562.2014.950046`.

Hussain, A.K.M.F., 1983. "Coherent structuresreality and myth". *The Physics of Fluids*, Vol. 26, No. 10, pp. 2816–2850. ISSN 0031-9171. doi:10.1063/1.864048.

Jones, O.C., 1976. "An improvement in the calculation of turbulent friction in rectangular ducts". *Journal of Fluids Engineering*, Vol. 98, No. 2, p. 173180. ISSN 1528-901X. doi:10.1115/1.3448250. URL `http://dx.doi.org/10.1115/1.3448250`.

Karamanos, G.S. and Karniadakis, G., 2000. "A spectral vanishing viscosity method for large-eddy simulations". *Journal of Computational Physics*, Vol. 163, No. 1, pp. 22–50. ISSN 0021-9991. doi:https://doi.org/10.1006/jcph.2000.6552.

Kravchenko, A. and Moin, P., 1997. "On the effect of numerical errors in large eddy simulations of turbulent flows". *Journal of Computational Physics*, Vol. 131, No. 2, pp. 310–322.

Lamballais, E., Fortuné, V. and Laizet, S., 2011. "Straightforward high-order numerical dissipation via the viscous term for direct and large eddy simulation". *Journal of Computational Physics*, Vol. 230, No. 9, pp. 3270–3275.

Lee, T. and Matescu, D., 1998. "Experimental and numerical investigation of 2-d backward-facing step flow". *Journal of Fluids and Structures*, Vol. 12, No. 6, pp. 703–716. ISSN 0889-9746. doi:https://doi.org/10.1006/jfls.1998.0166.

Lele, S.K., 1992. "Compact finite difference schemes with spectral-like resolution". *Journal of computational physics*, Vol. 103, No. 1, pp. 16–42.

Lesieur, M., Métais, O. and Comte, P., 2005. *Large-Eddy Simulations of Turbulence*. Cambridge University Press. doi:10.1017/CBO9780511755507.

Li, N. and Laizet, S., 2010. "2decomp&fft - a highly scalable 2d decomposition library and fft interface". In *Cray User Group 2010 conference*. pp. 1–13. URL `https://api.semanticscholar.org/CorpusID:62453043`.

Lien, F. and Leschziner, M., 1994. "Assessment of turbulence-transport models including non-linear rng eddy-viscosity formulation and second-moment closure for flow over a backward-facing step". *Computers & Fluids*, Vol. 23, No. 8, pp. 983–1004. ISSN 0045-7930. doi:https://doi.org/10.1016/0045-7930(94)90001-9.

Lu, H. and Zhao, W., 2018. "Numerical study of particle deposition in turbulent duct flow with a forward- or backward-facing step". *Fuel*, Vol. 234, pp. 189–198. ISSN 0016-2361. doi:https://doi.org/10.1016/j.fuel.2018.07.033.

Schuch, F.N., 2020. *Análise do mergulho de escoamentos hiperpicnais em canal inclinado por meio de simulação numérica de grandes escalas*. Ph.D. thesis, Pontifícia Universidade Católica do Rio Grande do Sul (PUCRS), Porto Alegre.

Tihon, J., Pnkavová, V. and Pantzali, M., 2010. "The effect of inlet pulsations on the backward-facing step flow". *European Journal of Mechanics - B/Fluids*, Vol. 29, No. 3, pp. 224–235. ISSN 0997-7546. doi: https://doi.org/10.1016/j.euromechflu.2010.02.001.

Zhang, J., Niu, X., Ye, L., Zhang, B., Shi, Q., Zhang, L. and Liu, C., 2024. "Effect of backward-facing step and turbulence level on film cooling characteristic of a turbine concave endwall with upstream leakage flow". *Applied Thermal Engineering*, Vol. 243, p. 122671. ISSN 1359-4311. doi:https://doi.org/10.1016/j.applthermaleng.2024.122671.

7. RESPONSIBILITY NOTICE

The authors are the only responsible for the printed material included in this paper.